buildings

MDPI

Article

Crack Detection in Bearing Plate of Prestressed Anchorage Using Electromechanical Impedance Technique: A Numerical Investigation

Ba-Tung Le [1,2], Thanh-Truong Nguyen [2,3], Tran-De-Nhat Truong [1,2], Chi-Thien Nguyen [1,2], Thi Tuong Vy Phan [4], Duc-Duy Ho [1,2,*] and Thanh-Canh Huynh [4,5,*]

1 Faculty of Civil Engineering, Ho Chi Minh City University of Technology (HCMUT), 268 Ly Thuong Kiet, District 10, Ho Chi Minh City 700000, Vietnam
2 Vietnam National University Ho Chi Minh City (VNU-HCM), Linh Trung Ward, Thu Duc City, Ho Chi Minh City 700000, Vietnam
3 Industrial Maintenance Training Center, Ho Chi Minh City University of Technology (HCMUT), 268 Ly Thuong Kiet Street, District 10, Ho Chi Minh City 700000, Vietnam
4 Institute of Research and Development, Duy Tan University, Danang 550000, Vietnam
5 Faculty of Civil Engineering, Duy Tan University, Danang 550000, Vietnam
* Correspondence: hoducduy@hcmut.edu.vn (D.-D.H.); huynhthanhcanh@duytan.edu.vn (T.-C.H.)

Abstract: The bearing plate is an important part of a tendon–anchorage subsystem; however, its function and safety can be compromised by factors such as fatigue and corrosion. This paper explores the feasibility of the electromechanical impedance (EMI) technique for fatigue crack detection in the bearing plate of a prestressed anchorage. Firstly, the theory of the EMI technique is presented. Next, a well-established prestressed anchorage in the literature is selected as the target structure. Thirdly, a 3D finite element model of the PZT transducer–target anchorage subsystem is simulated, consisting of a concrete segment, a steel anchor head, and a steel bearing plate instrumented with a PZT transducer. The prestress load is applied to the anchorage via the anchor head. The EMI response of the target structure is numerically obtained under different simulated fatigue cracks in the bearing plate using the linear impedance analysis in the frequency domain. Finally, the resulting EMI response was quantified using two damage metrics: root-mean-square deviation and correlation coefficient deviation. These metrics are then compared with a threshold to identify the presence of cracks in the bearing plate. The results show that the simulated cracks in the bearing plate are successfully detected by tracking the shifts in the damage metrics. The numerical investigation demonstrates the potential of the EMI technique as a non-destructive testing method for assessing the structural integrity of prestressed structures.

Keywords: EMI technique; bearing plate; crack detection; damage detection; FEM; PZT

Citation: Le, B.-T.; Nguyen, T.-T.; Truong, T.-D.-N.; Nguyen, C.-T.; Phan, T.T.V.; Ho, D.-D.; Huynh, T.-C. Crack Detection in Bearing Plate of Prestressed Anchorage Using Electromechanical Impedance Technique: A Numerical Investigation. *Buildings* **2023**, *13*, 1008. https://doi.org/10.3390/buildings13041008

Academic Editors: Marta Kaluza and Janusz Krentowski

Received: 1 March 2023
Revised: 5 April 2023
Accepted: 10 April 2023
Published: 11 April 2023

1. Introduction

The electromechanical impedance (EMI) technique has been extensively studied to detect damage in civil infrastructure [1–3]. Its practicality for structural health monitoring has been demonstrated by various real applications [4–8]. This technique involves attaching a small, inexpensive, high-sensitivity, and quick-responsiveness piezoelectric transducer, such as PZT (lead zirconate titanate), to the structure being monitored to measure EMI response [9]. By observing changes in the EMI response caused by damage, the integrity of the monitored structure can be evaluated. The main advantages of the technique can be summarized as follows: (i) it can be applied to a wide range of structures, including civil, aerospace, and mechanical systems; (ii) it is a low-cost technique and can be implemented in real time; (iii) it is highly sensitive to minor structural damages due to the use of the EMI response in a high-frequency band.

The tendon–anchorage subsystem of a prestressed structure plays an important role in transferring the prestress force to the entire structure. The failure of this vital subsystem can lead to the collapse of the whole prestressed structure [10]. The previous studies show that the EMI response of the prestressed anchorage is varied with changes in the prestress loss or local damage [11–13]. Over the past decade, the EMI technique has been studied as a cost-effective solution for monitoring prestress forces in anchorage subsystems [12,14–17]. In their study, Kim et al. [14] directly attached the piezoelectric transducer to the bearing plate of a prestressed concrete girder and successfully monitored the reduction in the prestress force by the EMI technique. They found that the frequency band sensitive to the prestress loss, from 800 to 1000 kHz, was relatively high [14]. Min et al. [12] established the relation between the EMI response and the prestress force to predict remaining tensions in a multi-strand prestressed system. Nguyen et al. [18] developed a deep learning-based regression model for estimating the prestress force of a prestressed concrete beam. Recently, Dang et al. [19] successfully monitored tension forces and detected loosened strands in a multi-strand anchorage using multiple PZT interfaces. Pham et al. [20,21] have developed PZT-based smart aggregates to detect inner concrete cracks in the prestressed anchorage. The above studies have verified the great potential of the EMI technique for the structural health monitoring of prestressed concrete structures.

The bearing plate is a critical component of the anchorage subsystem and potentially damaged by various factors such as fatigue and corrosion [11,22,23]; however, most of the previous studies have focused on using EMI response for monitoring the prestress force in the prestressed anchorage, and only a few studies have explored its application for crack detection in the bearing plate of the anchorage. Previous studies have examined the numerical simulation of the EMI technique for structural health monitoring in civil structures [16,24–28]; however, there has been no simulation research on crack detection in the bearing plate of a prestressed anchorage. This study aims to investigate the potential of the EMI technique for detecting cracks in the bearing plate of a prestressed anchorage via a numerical simulation. The paper commences by presenting the fundamental principles of the EMI technique and damage evaluation metrics. Then, a well-established prestressed anchorage from the literature is selected as the target structure [14]. This is a mono tendon–anchorage of a prestressed reinforced concrete (RC) beam, in which the prestress load is introduced into the beam via a single prestressing strand anchored at two ends by anchor heads and bearing plates. Subsequently, the feasibility of the proposed EMI technique is evaluated via finite element (FE) modeling, in which an FE model with vertical and horizontal fatigue cracks is simulated. Finally, the damage evaluation metrics are employed to estimate the change in the EMI response, thereby enabling the detection of fatigue cracks in the bearing plate.

2. EMI Technique

2.1. Overview

The schematic of the EMI technique for crack detection in a mono tendon–anchorage subsystem is depicted in Figure 1. The EMI technique is based on the principle of measuring the alternation in the mechanical impedance of a monitored structure caused by damage. The mechanical impedance is the ratio of the force applied to the structure to the resulting motion of the structure [29]. Any changes in the mechanical impedance can be an indication of damage in the structure [7]. To apply the EMI technique, a piezoelectric patch such as PZT are bonded to the surface of the bearing plate of the prestressed anchorage, as shown in Figure 1. The EMI response of the anchorage is then periodically measured in a predefined frequency band by an impedance analyzer with a harmonic voltage excitation. Next, statistical damage metrics are used to quantify the change in the EMI response. Finally, the structural integrity of the anchorage is assessed by the damage metrics. In the following sections, the fundamental of the EMI impedance and the damage evaluation methods are presented.

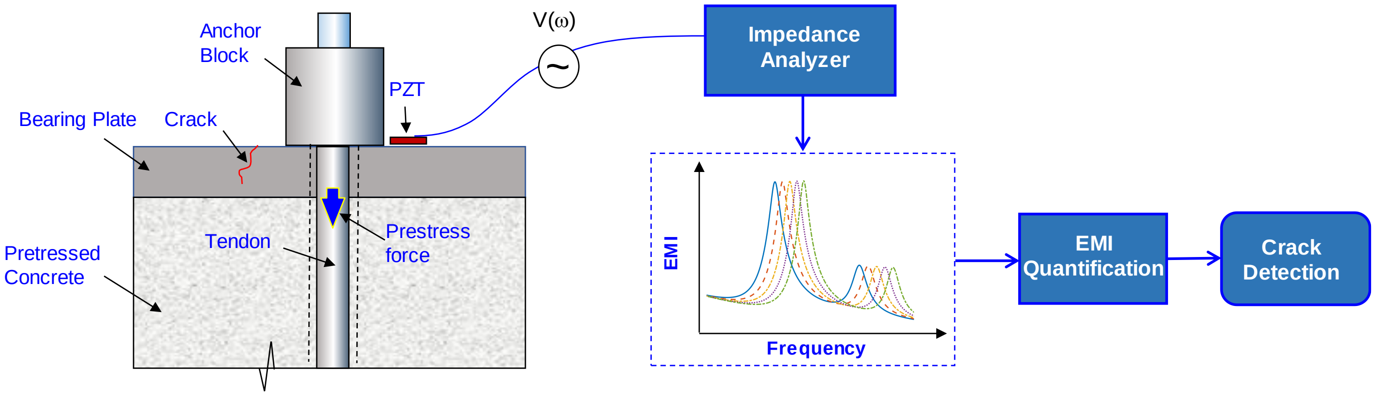

Figure 1. Overview of the EMI technique for crack detection in prestressed anchorage.

2.2. Theory of EMI Response

In the EMI technique, the PZT transducer is excited by a harmonic voltage $V(\omega)$ using an impedance analyzer. PZT is a piezoelectric material that can produce an electrical charge in response to a mechanical force or vice versa. As a result of the inverse piezoelectric effect, the voltage applied to the PZT transducer causes deformation, as shown in Figure 2a. This deformation, in turn, generates a force $F(\omega)$ at the PZT exciting point. The coupling between the PZT transducer and the host structure can be modeled as a 1-dof (degree-of-freedom) mass-spring-damper system, as shown in Figure 2b [30,31]. Dividing the force ($F(\omega)$) by the velocity $(\dot{u}(\omega))$ of the host structure at the driving point of the PZT yields the mechanical impedance of the monitored structure ($Z_s(\omega)$), as presented in [29]:

$$Z_s(\omega) = \frac{F(\omega)}{\dot{u}(\omega)} = c + m\frac{\omega^2 - \omega_n^2}{\omega}i \tag{1}$$

in which m, c, and k are the mass, the damping coefficient, and the stiffness constant of the host structure, respectively. The term i represents the imaginary unit, while ω_n refers to the monitored structure's natural frequency, and ω denotes the sweep frequency of the PZT transducer.

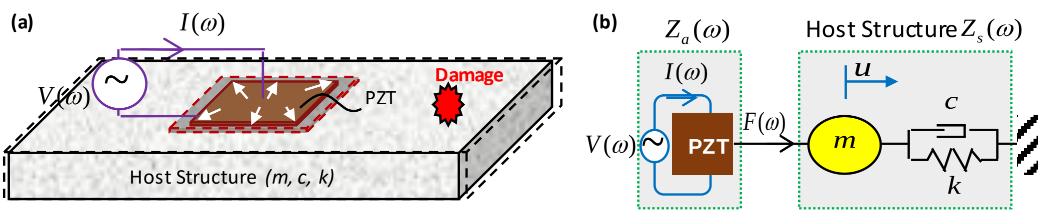

Figure 2. The PZT–structure interactive system: (**a**) PZT's expansion under applied voltage; (**b**) simplified impedance model.

The EMI response of the 1-dof system is determined as a combined function of the mechanical impedance of the monitored structure ($Z_s(\omega)$) and that of PZT ($Z_a(\omega)$), according to the following equation [7]:

$$Z(\omega) = \frac{V(\omega)}{I(\omega)} = \left\{ i\omega\frac{w_a l_a}{t_a}\left[\hat{\varepsilon}_{33}^T - \frac{1}{Z_a(\omega)/Z_s(\omega)+1}d_{3x}^2\hat{Y}_{xx}^E\right]\right\}^{-1} \tag{2}$$

In Equation (2), $\hat{Y}_{xx}^E$ represents the complex Young's modulus of the PZT transducer under zero electric field; $\hat{\varepsilon}_{xx}^T$ stands for the complex dielectric constant under zero stress; d_{3x} denotes the piezoelectric coupling constant in the x-direction under zero stress; and w_a, l_a, and t_a indicate the width, length, and thickness of the PZT transducer, respectively.

By combining Equations (1) and (2), it is possible to interpret information about the mass, the damping coefficient, and the stiffness constant (m, c, and k) of the monitored structure from its EMI response [32,33]. Any damage to the structure will result in an alternation in the EMI response, which can be detected by impedance monitoring. In practice, it is important to capture EMI responses within a specific high-frequency range. Due to the short wavelengths generated by the PZT's excitation at a high frequency, the EMI technique can effectively detect minor structural damages [7].

2.3. Damage Evaluation Approach

In order to achieve reliable damage detection, it is essential to select an appropriate damage metric. The appropriateness of an evaluation metric can vary depending on the specific structure being studied, as a metric that may be effective for one structure may not work well for another. We selected two damage indices: Root Mean Square Deviation (*RMSD*) and Cross-Correlation Coefficient Deviation (*CCD*), which are widely employed to quantify the changes in impedance signatures [1,2]. It is noted that the *RMSD* and *CCD* metrics differ in their sensitivity to structural damage. The *CCD* evaluation metric is defined as [9,34]

$$CCD = 1 - \frac{1}{N-1}\frac{\sum_{i=1}^{N}\left(Z(\omega_i)-\overline{Z}\right)\left(Z^*(\omega_i)-\overline{Z}^*\right)}{\sigma_Z\sigma_{Z^*}} \tag{3}$$

According to the references [2,35], the *RMSD* evaluation metric can be obtained by the following equation:

$$RMSD = \sqrt{\frac{\sum_{i=1}^{N}\left[Z^*(\omega_i)-Z(\omega_i)\right]^2}{\sum_{i=1}^{N}\left[Z(\omega_i)\right]^2}} \tag{4}$$

In the Equations (3) and (4), $Z(\omega_i)$ represents the EMI signature at the healthy state for the ith frequency; $Z^*(\omega_i)$ stands for the EMI signature at the unknown state, N, which indicates the number of scanned frequencies; $\overline{Z}$ and $\overline{Z}^*$ represent the means of the EMI signatures; and the symbols σ_Z and σ_Z^* are the standard deviations.

The *RMSD* and *CCD* indices will be greater than 0 in response to the presence of damage. The selection of an appropriate damage index depends on the variation trend of the impedance. While the *CCD* metric is more responsive to frequency changes and less sensitive to amplitude changes in the EMI response, the *RMSD* metric is sensitive to both types of changes [36,37]. Selecting an unsuitable damage metric may lead to suboptimal outcomes in detecting damage and estimating its severity. In this study, both *RMSD* and *CCD* metrics are examined to evaluate their effectiveness in detecting cracks in the bearing plate of prestressed anchorage.

3. Numerical Simulation

3.1. Description of Target Structure

The target structure is the prestressed anchorage of a T-shaped RC beam, which is a mono tendon–anchorage, as presented in the previous study [14]. Figure 3 illustrates the target structure's geometry and dimensions, following the experimental model's realistic geometry. As depicted in Figure 3a, the beam is simply supported on two steel bars with overhangs of 0.2 m. The beam is prestressed by a load of 14 tons using a seven-wire steel strand of 15.2 mm. The strand is enclosed in a plastic duct with a diameter of 25 mm and secured at its two ends by two bearing steel plates. As depicted in Figure 3b, the beam's cross-section is T-shaped with a flange width of 0.71 m and a height of 0.6 m. As illustrated in Figure 3c, the dimensions of the steel anchor head are 45 mm in diameter and 45 mm in height. To acquire the EMI response from the prestressed anchorage, the PZT transducer is installed on the bearing plate right below the anchor head, as illustrated in Figure 3a. The PZT patch has a square shape with a size of 10 × 10 × 0.508 mm, as sketched in Figure 3d. Figure 3e–g present the geometric parameters of the bearing plate in the top, front, and back views.

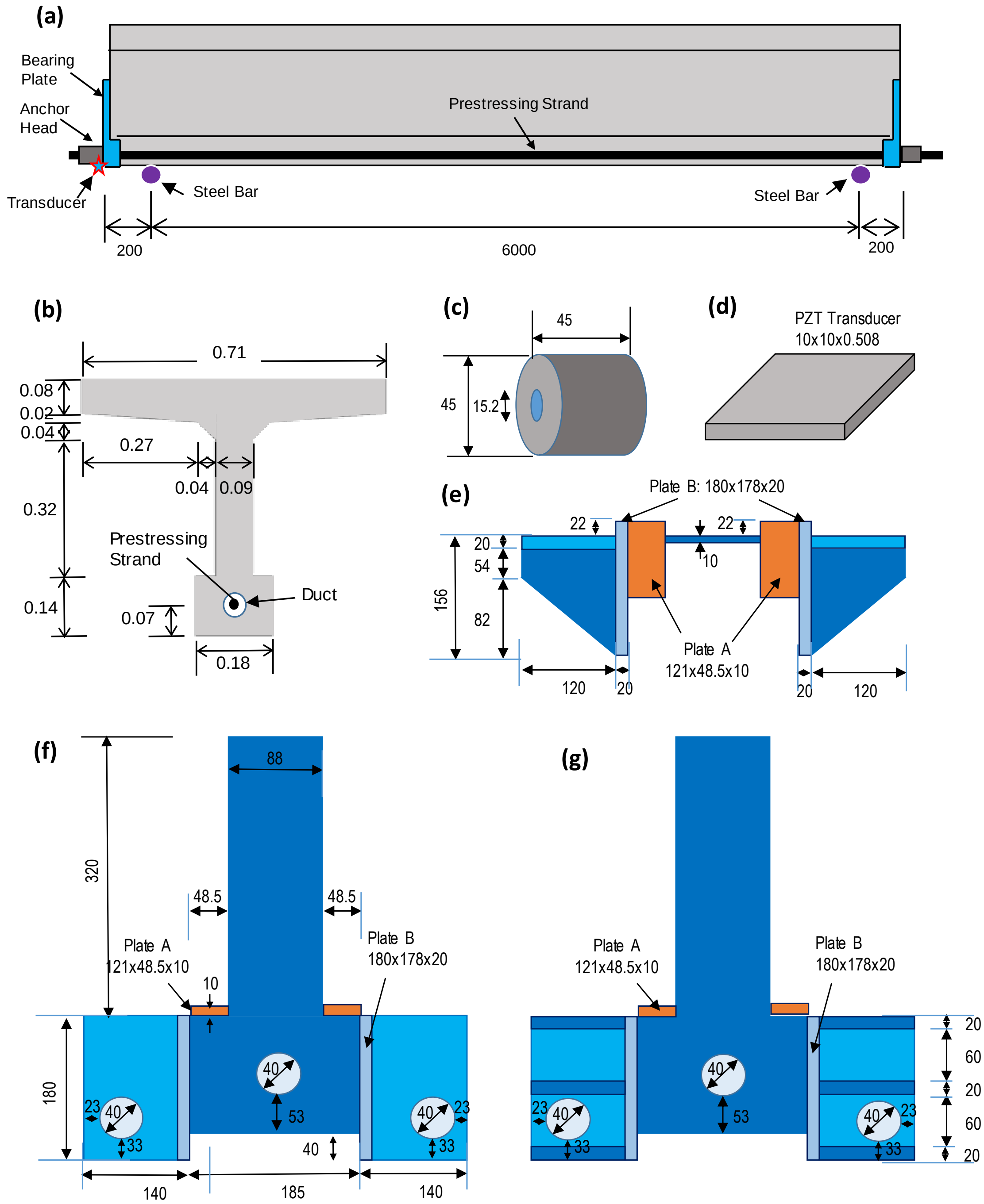

Figure 3. Geometry and dimensions of the target structure: (**a**) Prestressed RC beam; (**b**) cross-section of the beam; (**c**) anchor head; (**d**) PZT transducer; (**e**) top view, (**f**) front view and (**g**) back view of the bearing plate.

3.2. Finite Element Modeling

To accurately simulate the piezoelectric effects of the PZT-anchorage subsystem, it is necessary to account for both electrical and mechanical physics that act simultaneously during PZT's harmonic excitation [38–40]. Given its robust modeling capabilities for piezoelectric effects [16,41–43], the finite element (FE) modeling program, COMSOL Multiphysics, was adopted to simulate the EMI response of the target anchorage. The FE modeling procedure of the EMI response used in this study followed the protocol presented in the previous studies [16,25,42].

3.2.1. Structural and Material Modeling

The simulated part is the 0.2 m overhang of the prestressed RC beam, as shown in Figure 4a. The FE model consists of an RC segment, a bearing plate embedded with a PZT transducer, and an anchor head. The geometric parameters of all structural members in the FE model followed the previous experimental model [14], as illustrated in Figure 3. In the structural modeling, all structural members were formed into a union. A prestress load of 10 tons was applied on the anchor head in a direction perpendicular to the bearing plate, as illustrated in Figure 4b. A fatigue crack was simulated in the bearing plate, which was supposed to be on the right of the anchor head. The crack was simulated by removing the material of the bearing plate. The PZT transducer was positioned right below the anchor head with a distance between them of 11.5 mm.

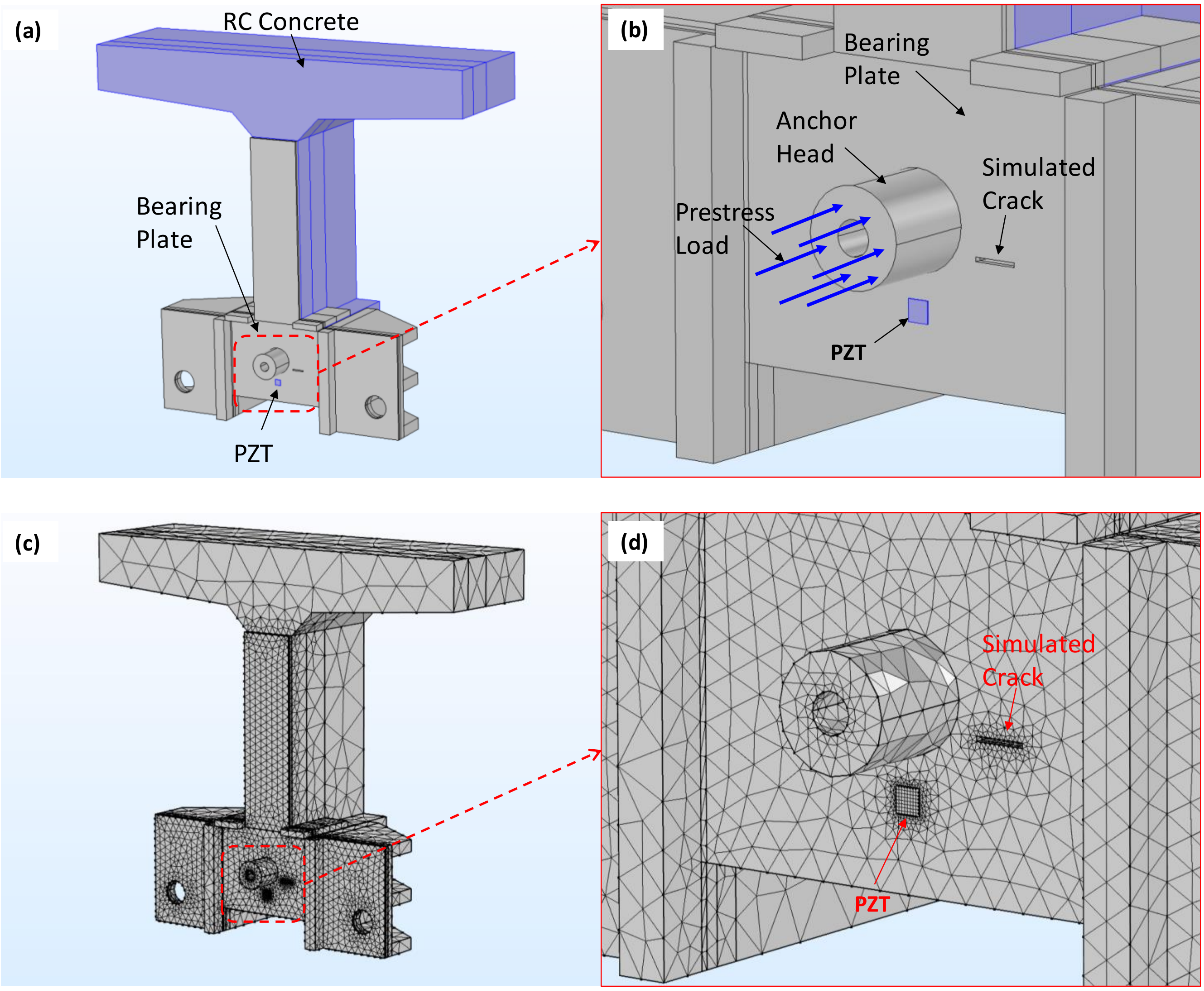

Figure 4. 3D simulation of the PZT–anchorage subsystem: (**a**) FE model; (**b**) anchorage; (**c**) meshed FE model; (**d**) meshing at anchorage.

In the material modeling, the bearing plate and the anchor head were assigned by steel materials with mechanical properties, as presented in Table 1 [14,16]. In addition, the PZT transducer was assigned by the PZT-5A material with piezoelectric properties, as presented in Table 2 [16]. The material properties of the RC concrete segment were also presented in Table 1 [14]. The FE model was discretized by employing the controlled meshing capability option for users available in COMSOL, as presented in Figure 4c. The mesh size was gradually reduced until the resulting EMI signature remained nearly constant, using the method described in a previous study [25]. A finer mesh was applied to the PZT transducer and simulated crack, as illustrated in Figure 4d. The total number of elements was 31,665, consisting of 64 hexahedral elements, 64 pyramid elements, and 31,537 tetrahedral elements.

Table 1. The mechanical properties of the structural elements in the FE model.

Parameters	Symbols	Steel Anchor Head and Steel Bearing Plate	RC Beam	Unit
Modulus	E	200	24.55	GPa
Poisson's ratio	ν	0.3	0.38	
Mass density	ρ	7850	2400	kg/m^3
Damping ratio	ξ	0.01	0.04	

Table 2. The piezoelectric properties of the PZT transducer.

Properties	Symbols	Value	Unit
Compliance matrix	$s_{11}^E = s_{22}^E$ s_{33}^E $s_{44}^E = s_{55}^E$ s_{66}^E $s_{12}^E = s_{21}^E$ $s_{13}^E = s_{31}^E$ $s_{23}^E = s_{32}^E$	16.4 18.8 47.5 44.3 −5.74 −7.22 −7.22	$\times 10^{-12}$ (m^2/N)
Coupling matrix	d_{31} d_{32} d_{33} d_{24} d_{15}	−171 −171 374 584 584	$\times 10^{-12}$ (C/N)
Relative permittivity	s_{11}^T s_{22}^T s_{33}^T	1730 1730 1730	
Mass density	ρ	7750	(kg/m^3)
Dielectric loss factor	δ	0.02	
Damping loss factor	η	0.02	

3.2.2. Compatibility and Boundary Conditions

In the simulations, the Solid Mechanics module and the Piezoelectric Device module of COMSOL Multiphysics were coupled to simulate the EMI response of the bearing plate. To ensure accurate modeling, the following compatibility conditions were taken into account: (i) continuity of displacements—the displacement field in the elastic and piezoelectric materials must be continuous across their interfaces with no gaps or overlaps between the materials; (ii) continuity of stresses—the stress field in the materials must also be continuous across their interfaces with no singularities at the interfaces; (iii) electrode compatibility—the electrodes used to apply the electric field in the piezoelectric material must be compatible with the material; (iv) charge conservation—the total charge in the piezoelectric material must be conserved by ensuring that the divergence of the electric displacement field is equal to the charge density; (v) electric field continuity—the electric field in the piezoelectric material must be continuous across the interfaces to avoid any abrupt changes in the field.

In the Solid Mechanics module, a fixed boundary was applied to the back side of the RC part to secure the structural condition of the overhang part of the prestressed RC beam. An electrical potential boundary condition was applied to the PZT transducer in the Piezoelectric Device module. Specifically, the PZT transducer's upper surface was assigned by the electrical potential of 1V, while the lower surface was set as the ground electrode. This simulation setup was similar with the previous studies [14,42].

3.2.3. Linear Stress Analysis under Prestress Load and Piezoelectric Deformation

Figure 5a illustrates the von Mises stress of the bearing plate when subjected to the prestress load of 10 tons (98.1 kN). To ensure that the prestressing effect is clearly observable, the color legend bar was set within a range of (0–5 $\times$ 10^7). The results indicate that stress concentration occurs around the anchor head, which can lead to the overloading of the surrounding material and result in cracks and other forms of damage. Hence, it is crucial to monitor the bearing plate's area around the anchor head to prevent potential failure.

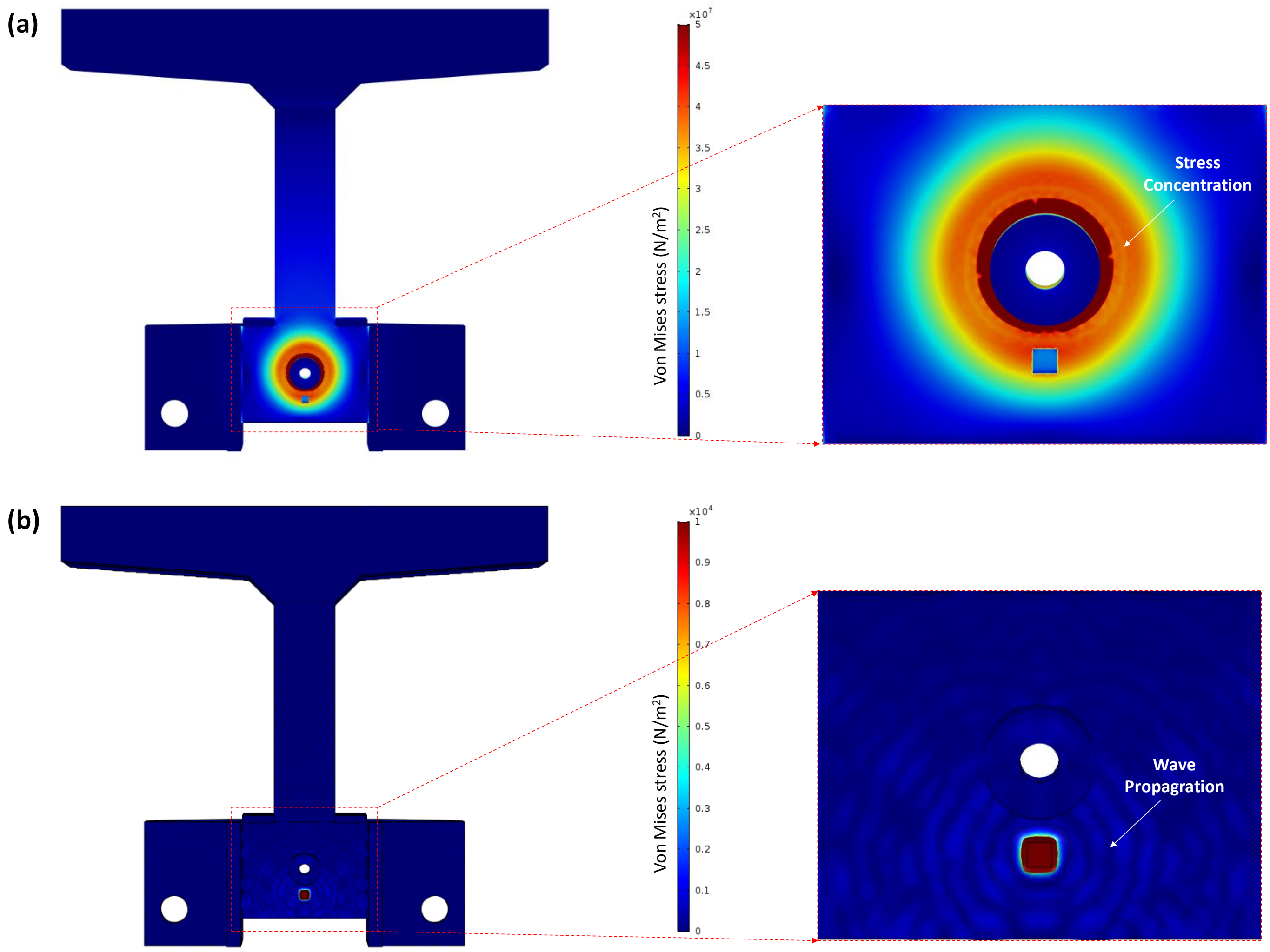

Figure 5. Von Mises stress under (**a**) prestress load and (**b**) PZT's excitation at 140 kHz.

Figure 5b presents the von Mises stress of the bearing plate under the PZT's excitation at 140 kHz. The color legend bar was set within a range of (0–1 $\times$ 10^4) to distinctly observe the presence of stress waves. It can be seen that the PZT transducer was expanded under the piezoelectric effect and its harmonic expansion induced an exciting force acting on the surface of the bearing plate at the driving point. As shown in Figure 5b, the stress waves were generated at the transducer's driving point and radially propagated into the bearing plate. The von Mises stress under the effect of stress waves (see Figure 5b) was inconsiderable compared to the effect of the prestress load (see Figure 5a).

3.3. Simulation of EMI Response under Fatigue Crack

The EMI response was investigated for a frequency band ranging from 10 kHz to 500 kHz (i.e., the sweep frequency band of the PZT transducer). At each frequency point, the resulting current from piezoelectric effects was simulated. The EMI response was then calculated numerically as the ratio between the applied voltage and the resulting current. It is important to note that when the frequency of the PZT's excitation matches the natural frequency of the monitored structure (i.e., the resonance frequency), the mechanical impedance of the system dominates the overall EMI response. Specifically, at resonance frequency, the damping coefficient (represented as $Z_s(\omega) = c$ in Equation (1)) of the host structure is the primary contributor to the overall EMI response ($Z(\omega)$ in Equation (2)). As the bearing plate undergoes cracking, both the modal damping and the stiffness of the plate are altered, leading to changes in both the frequency and magnitude of the impedance function at resonance. These changes in the EMI signature can be used to indicate the presence and severity of the crack in the bearing plate.

In the intact case, the anchorage was assumed to be healthy, not cracked. In the damage cases, two scenarios of cracking in the bearing plate were simulated, as shown in Figure 6. In the first scenario, as shown in Figure 6a, the horizontal fatigue crack with a size of 20 × 2 × 10 mm (width × height × depth) was simulated. The position of the horizontal crack is determined by the coordinates x and y. Five cases of the horizontal crack were investigated, including Case H1 (x = 17.5 mm; y = 0), Case H2 (x = 17.5 mm; y = 12.5 mm), Case H3 (x = 17.5 mm; y = 25 mm), Case H4 (x = 17.5 mm; y = 37.5 mm), and Case H5 (x = 17.5 mm; y = 62.5 mm). In the second scenario, the vertical fatigue crack was simulated, as shown in Figure 6b. The size of the vertical crack is the same as the horizontal crack. Four cases of the vertical crack were investigated, including Case V1 (x = 17.5 mm; y = 0), Case V2 (x = 17.5 mm; y = 25 mm), Case V3 (x = 17.5 mm; y = 50 mm), and Case V4 (x = 17.5 mm; y = 75 mm). It is noted that the positions of all simulated cracks were mostly within the stress concentration region of the bearing plate (see Figure 6a).

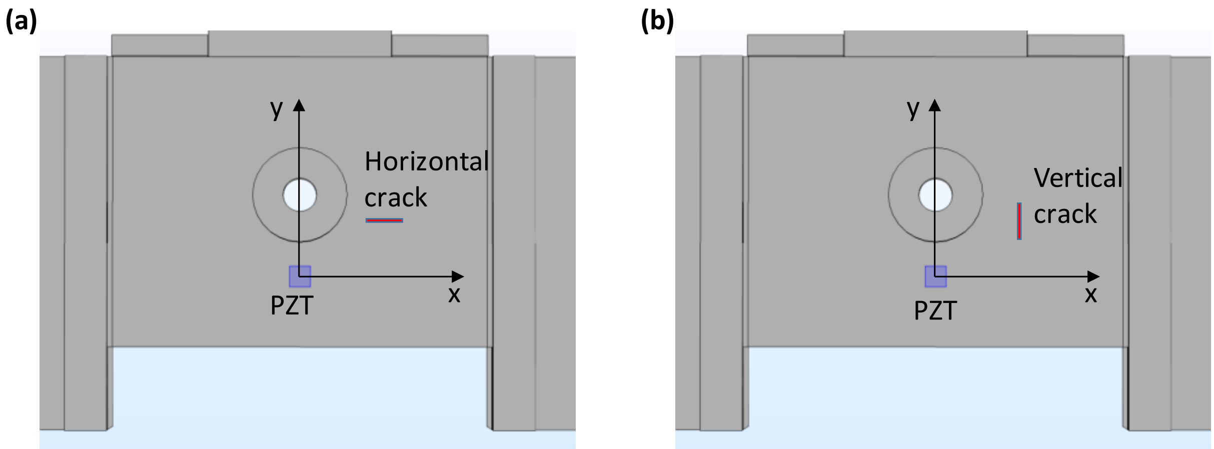

Figure 6. Simulation of cracks in the bearing plate: (**a**) Horizontal crack; (**b**) vertical crack.

Figure 7a presents the EMI response of the anchorage subjected to horizontal crack cases H1–H5. The EMI signatures above 50 kHz contain various resonant peaks, representing different local dynamics of the bearing plate. These resonant peaks changed in frequency and magnitude after the bearing plate was cracked, as shown in Figure 7b.

Moreover, the frequency band above 50 kHz showed significant variation while the band below 50 kHz remained stable. Figure 8a depicts the EMI response of the anchorage under vertical crack cases V1–V5. The EMI response varied as the bearing plate experienced a vertical fatigue crack. Similarly, the frequency band above 50 kHz showed more variations than the band below 50 kHz, as shown in Figure 8b. From the above observations, the frequency range of 50–100 kHz was selected as the sensitive frequency band for detecting the horizontal and vertical cracks in the bearing plate.

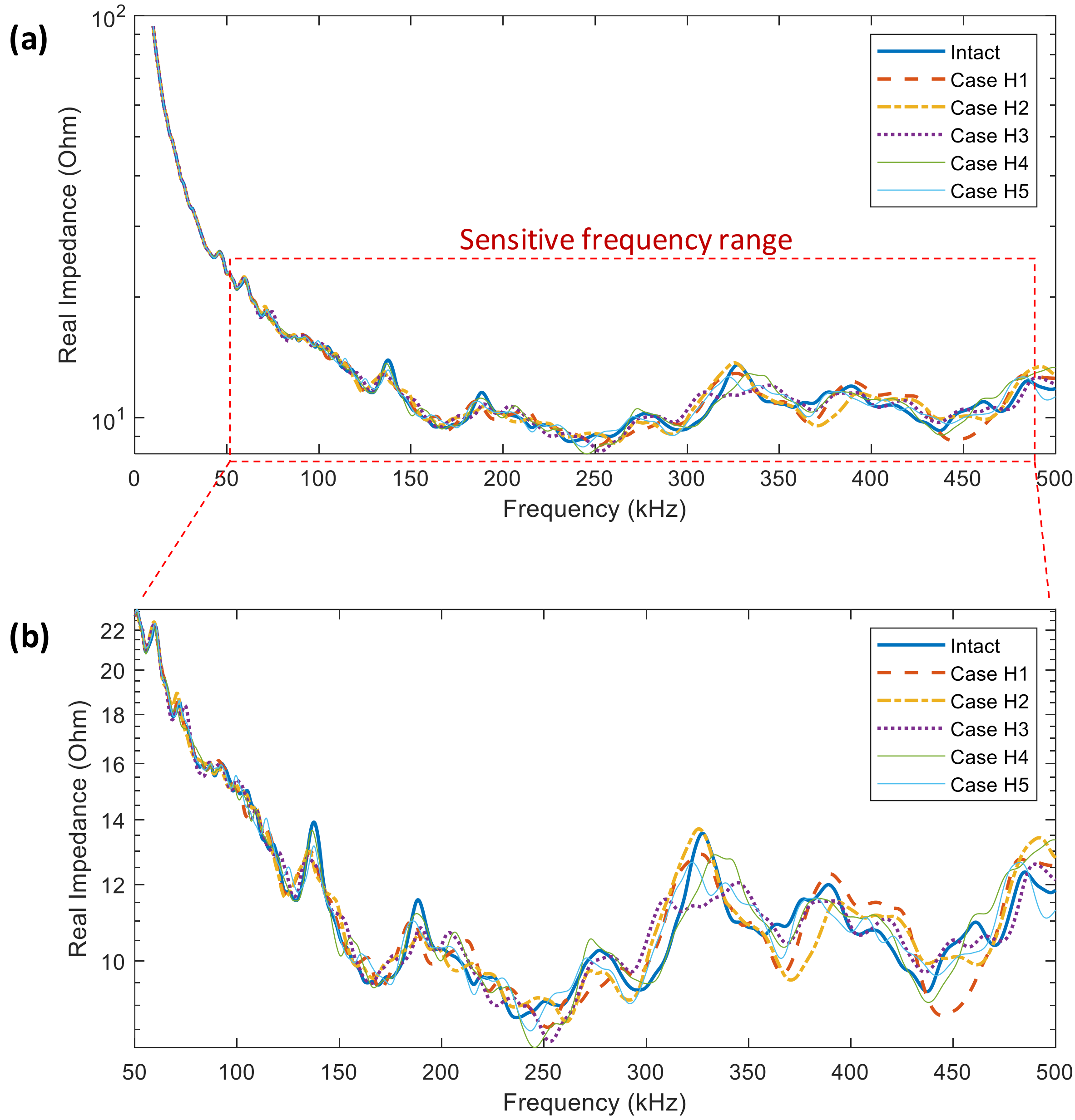

Figure 7. The EMI response of the anchorage under the intact case (not cracked) and horizontal crack cases: (**a**) Frequency range of 10–500 kHz; (**b**) sensitive frequency range of 50–500 kHz.

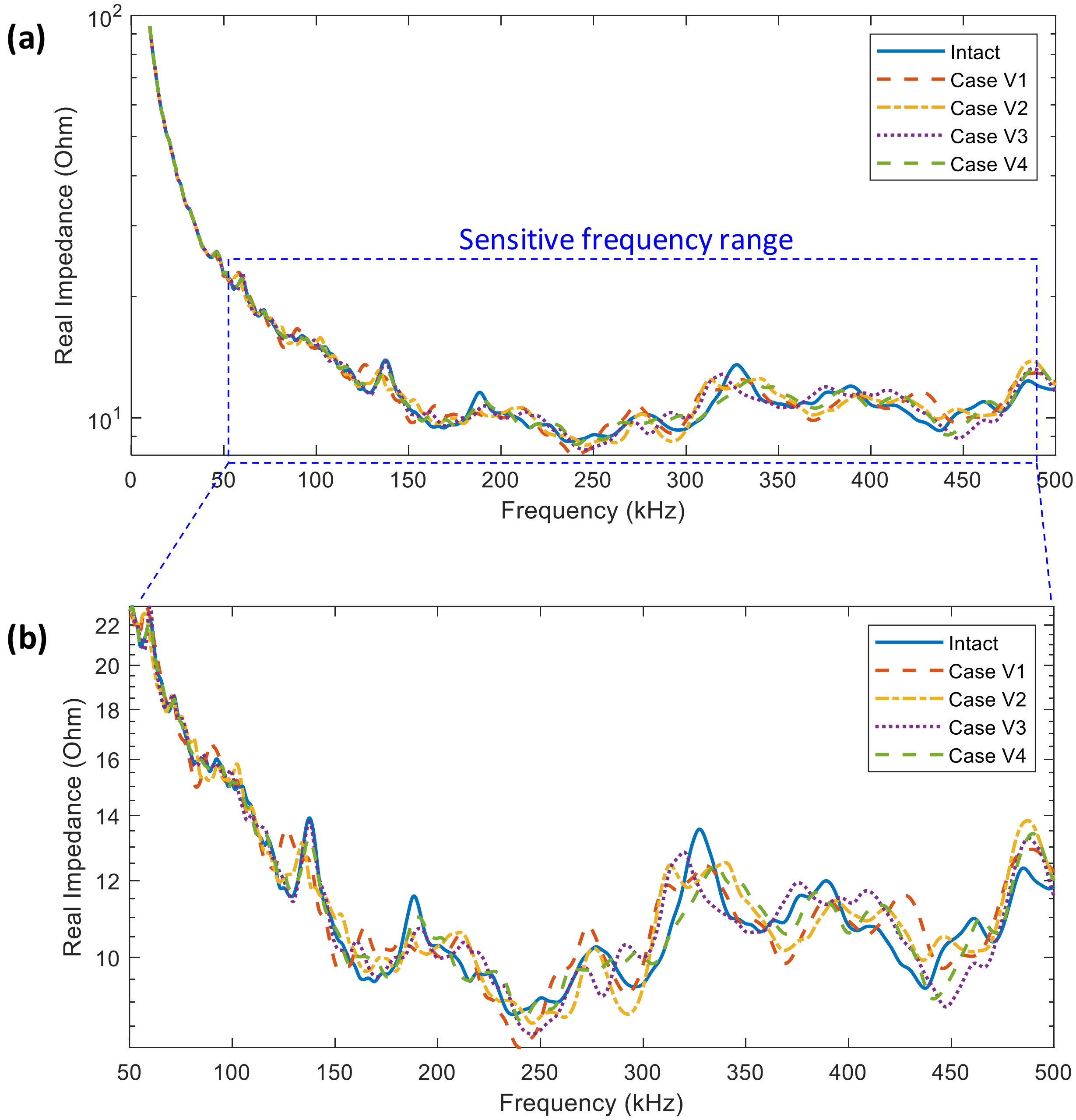

Figure 8. The EMI response of the anchorage under the intact case (not cracked) and vertical crack cases: (**a**) Frequency range of 10–500 kHz; (**b**) sensitive frequency range of 50–500 kHz.

3.4. EMI Quantification and Crack Assessment

We computed two damage indices, *CCD* and *RMSD*, to assess the changes in the EMI response caused by horizontal and vertical cracks. The full sensitive frequency band of 50–500 kHz with multiple resonant EMI peaks was used to compute these metrics, as suggested in the previous study [7]. Figure 9a,b depict the *CCD* and *RMSD* metrics for the cases of horizontal cracks, respectively. Both metrics showed negligible magnitudes for the intact case, but significant ones for the damage cases (H1–H5), indicating that the horizontal cracks were successfully detected. The magnitude of the *RMSD* metric was more significant than that of the *CCD* metric because the EMI response exhibited not only vertical shifts but also horizontal shifts due to the crack. Similarly, Figure 10a,b show the *CCD* and *RMSD* metrics for the cases of vertical cracks, respectively. Both metrics showed negligible magnitudes for the intact case, but significant ones for the damage cases (V1–V4), indicating the successful detection of the vertical cracks. Moreover, the *RMSD* metric exhibited higher magnitudes than the *CCD* metric.

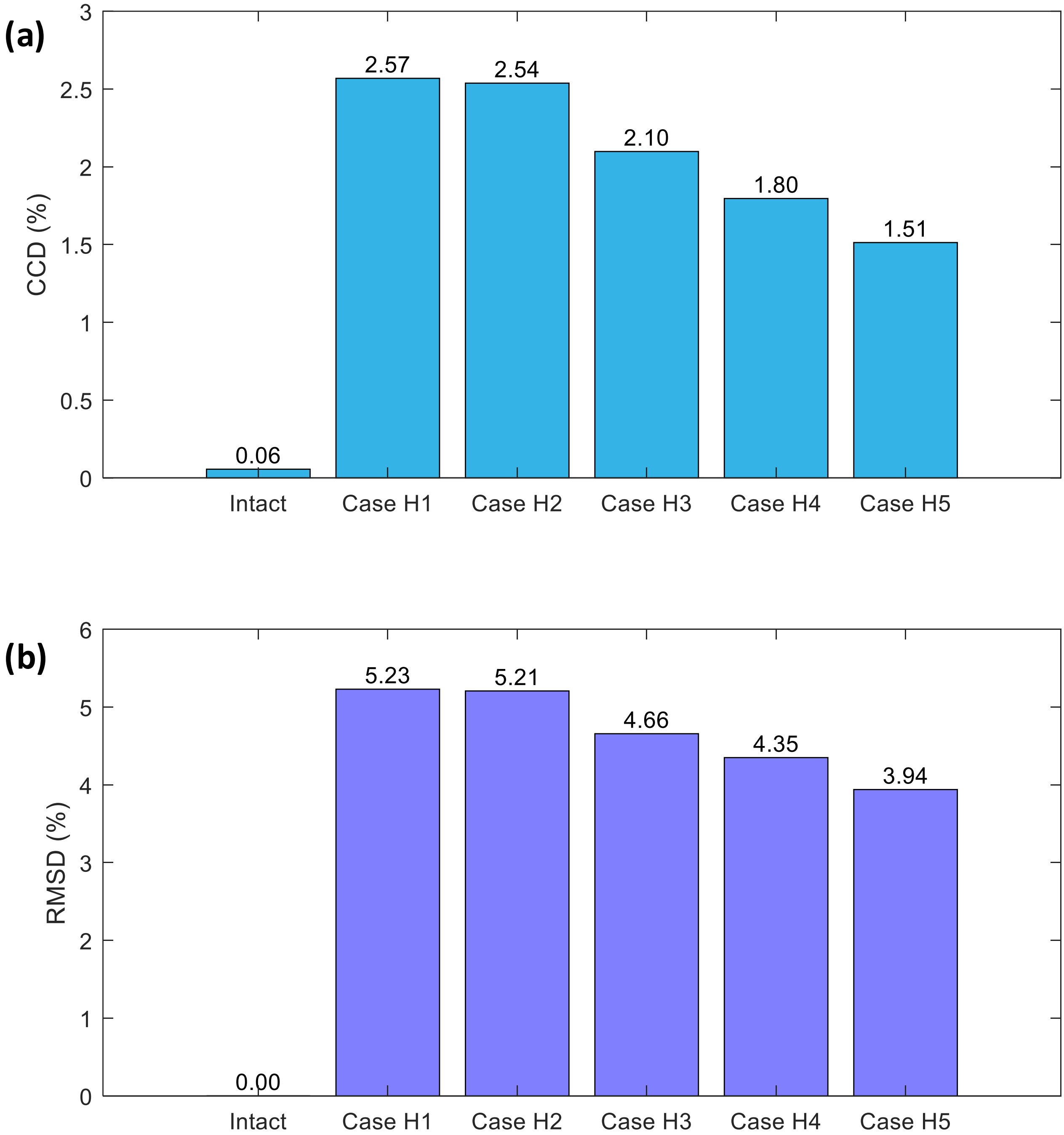

Figure 9. The quantification of the EMI change under the horizontal cracks using (**a**) *CCD* index and (**b**) *RMSD* index.

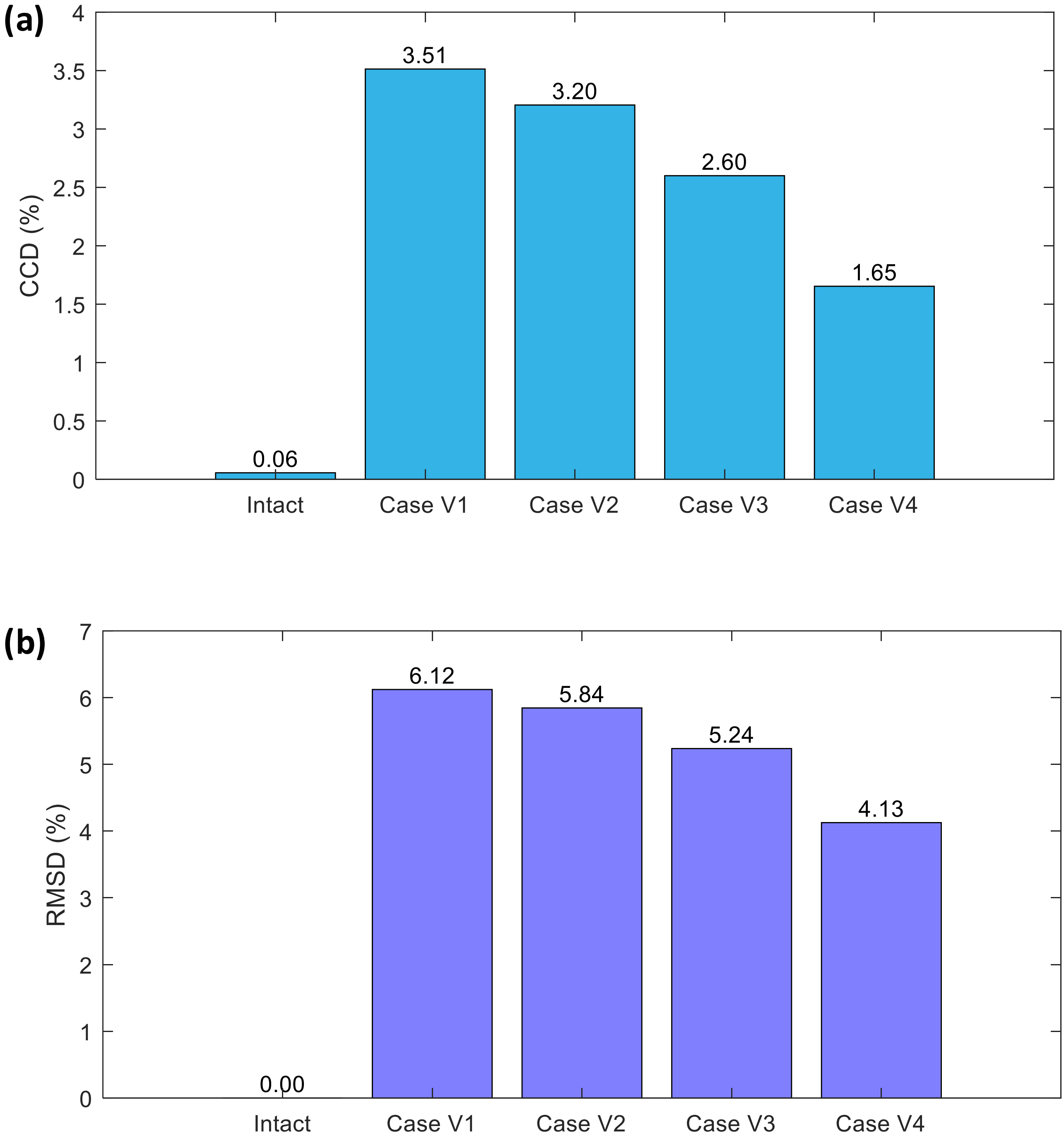

Figure 10. The quantification of the EMI change under the vertical cracks using (**a**) *CCD* index and (**b**) *RMSD* index.

Linear approximation functions were used to analyze the relationships between the location of the crack and the *RMSD* and *CCD* damage metrics. The result for the cases of horizontal cracks is depicted in Figure 11. Both RSMD and *CCD* datasets fit well with the linear lines, and the R-squared value accounted for 0.95 and 0.94 for the RSMD and *CCD* datasets, respectively. The metrics decreased as the distance from the transducer to the crack increased. Figure 12 shows the result for the cases of vertical cracks. The R-squared value was 0.93 for the *RMSD* metric and 0.95 for the *CCD* metric. It can be seen that both damage metrics showed a linear decrease with the sensing distance. This implies that the sensitivity of the EMI signature to the damage decreased when the sensing distance increased, which is consistent with the previous experimental observations [7,41].

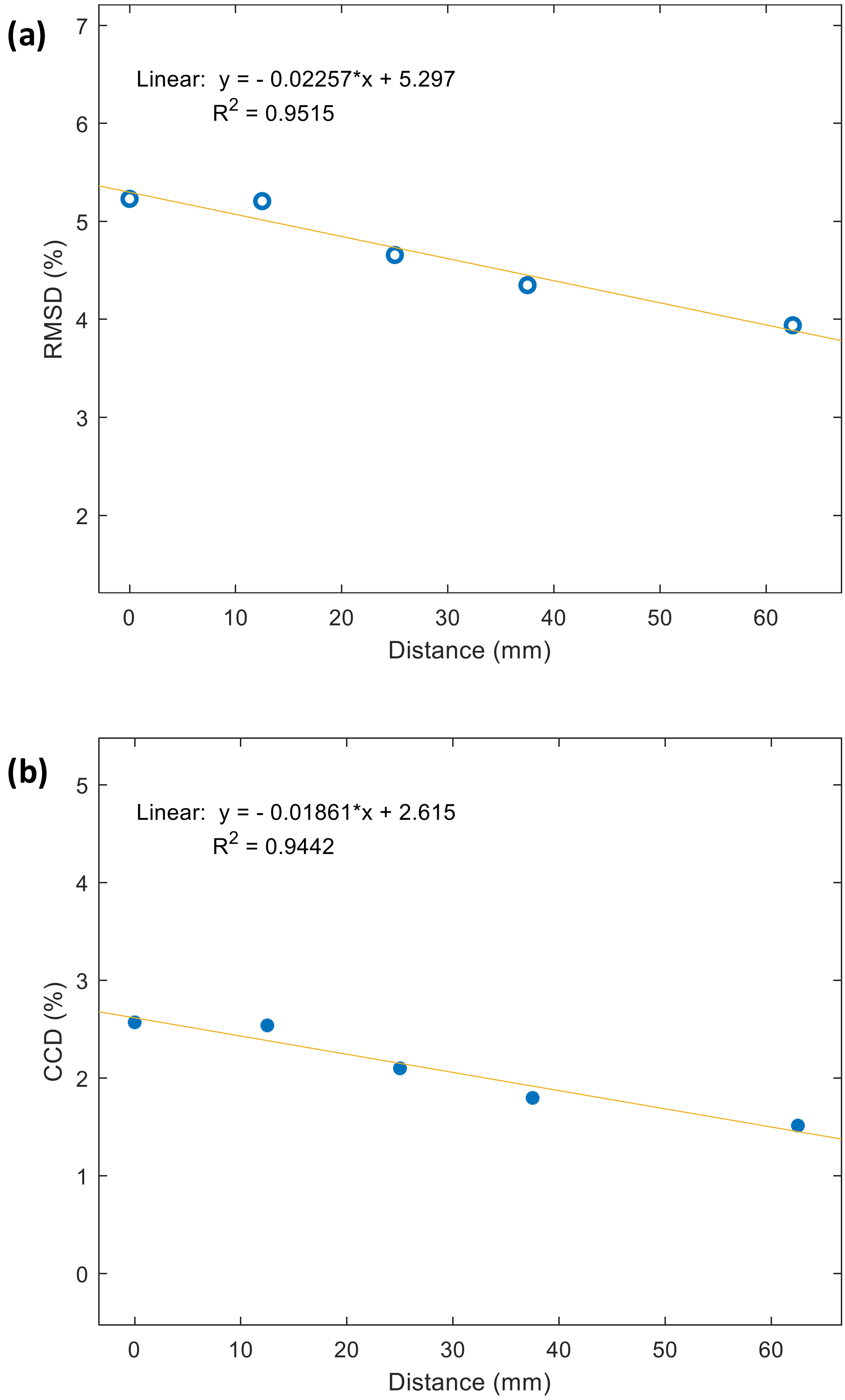

Figure 11. Linear regression analyses of the damage metric vs. the distance (y) for the horizontal cracks: (**a**) *RMSD* metric; (**b**) *CCD* metric.

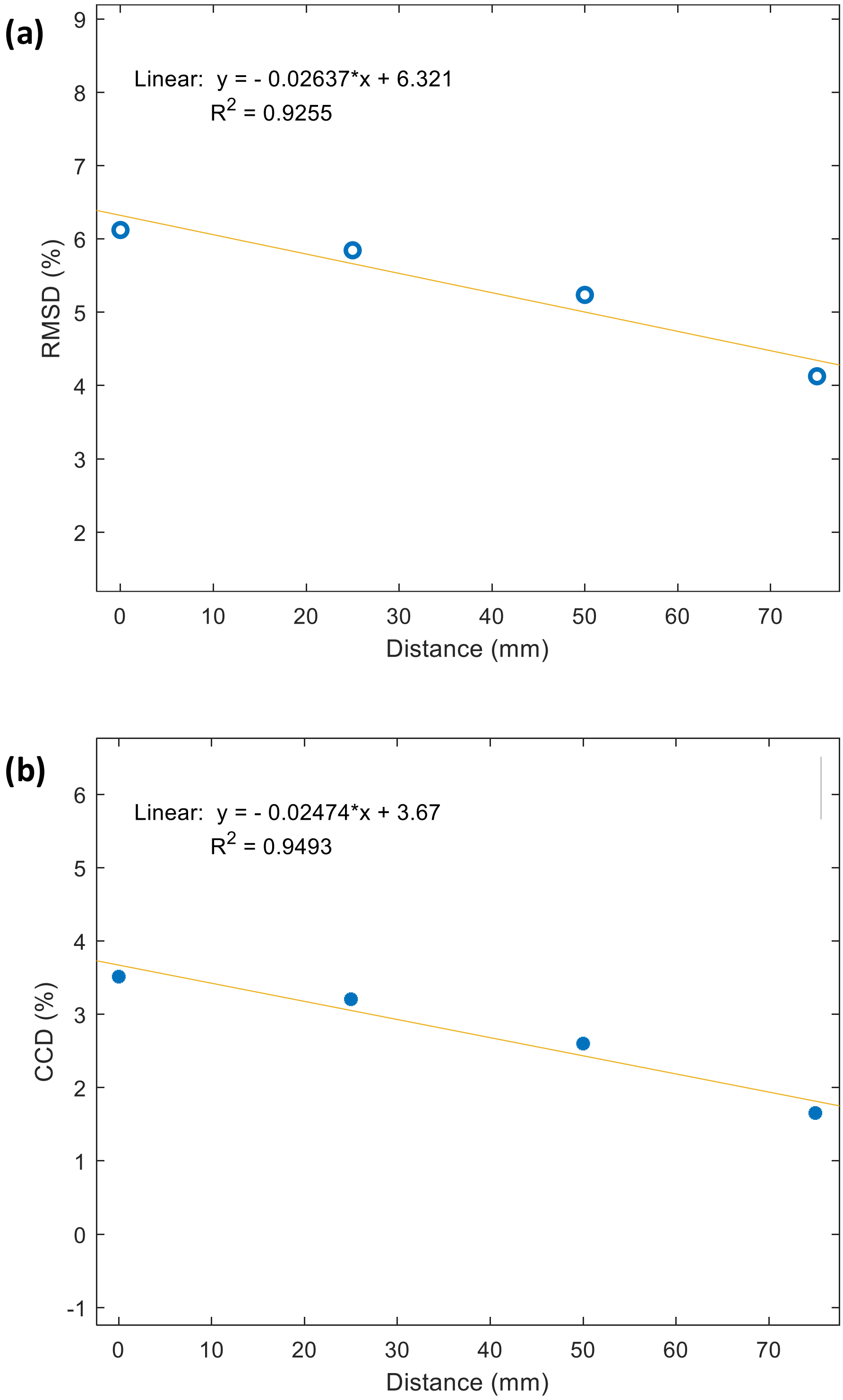

Figure 12. Linear regression analyses of the damage metric vs. the distance (y) for the vertical cracks: (**a**) *RMSD* metric; (**b**) *CCD* metric.

The numerical evaluation showed the effectiveness of the EMI method in detecting the presence of cracks in the bearing plate of prestressed structures. In addition to crack detection, the method can be utilized to predict the location of the cracks in the bearing plate. This can be achieved by performing regression analysis on the damage metric datasets obtained from various locations on the bearing plate. The resulting regression model is then used to estimate the location of the crack based on the metric obtained from the EMI measurements. Combining wireless sensor nodes with intelligent monitoring software [43–46], this method has a great promise to enhance the efficiency of crack detection in the bearing plate of a prestressed structure since it can allow for the remote identification of cracks without the need for on-site inspection by a human. Further research is needed to validate the effectiveness of this approach and to optimize the regression models used to predict the location of cracks.

4. Summary and Conclusions

The bearing plate of the prestressed anchorage is an important component that can be damaged by various factors such as fatigue and corrosion. This study investigated the numerical feasibility of the EMI technique for detecting cracks in the bearing plate of prestressed anchorage. Firstly, the EMI technique's fundamental principles and damage evaluation metrics were presented. Next, a well-established prestressed anchorage in the previous experiment was selected as the target structure. An FE model of the target anchorage with fatigue cracks in the bearing plate was simulated. Both vertical and horizontal cracks were considered to demonstrate the EMI method's effectiveness. Finally, the *RSMD* and *CCD* metrics were employed to quantify the change in the EMI response and to evaluate the bearing plate's structural integrity.

From the numerical evaluation, the following concluding remarks have been drawn:

(1) The EMI response above 50 kHz showed high sensitivity to cracks in the bearing plate.
(2) The bearing plate's vertical and horizontal cracks were successfully detected using the *RMSD* and *CCD* metrics.
(3) The relationship between the damage metrics and the sensing distance was linear: the magnitude of damage metrics linearly decreased with the sensing distance.

The numerical investigation shows the great promise of the EMI technique as a non-destructive testing method for assessing the structural integrity of prestressed structures. The FE modeling technique presented in this study can be used to optimize the transducer placement and predict crack severity for practical applications. In the future, lab-scale and field-scale experiments will be conducted to verify the practicality of the proposed EMI technique. In addition, advanced regression models will be developed to predict crack locations and estimate crack severity.

Author Contributions: Conceptualization, T.-C.H. and D.-D.H.; methodology, T.-C.H., D.-D.H. and B.-T.L.; validation, T.-C.H., D.-D.H., B.-T.L. and T.-T.N.; formal analysis, T.-C.H., T.-T.N., T.-D.-N.T. and C.-T.N.; writing—original draft preparation, T.-C.H., D.-D.H. and B.-T.L.; writing—review and editing, T.T.V.P., T.-C.H. and D.-D.H. All authors have read and agreed to the published version of the manuscript.

Funding: This research received no external funding.

Data Availability Statement: The data are available upon request.

Acknowledgments: We acknowledge Ho Chi Minh City University of Technology (HCMUT), VNU-HCM for supporting this study.

Conflicts of Interest: The authors declare no conflict of interest.

References

1. Song, G.; Gu, H.; Mo, Y.-L. Smart aggregates: Multi-functional sensors for concrete structures—A tutorial and a review. *Smart Mater. Struct.* **2008**, *17*, 033001. [CrossRef]
2. Na, W.S.; Baek, J. A Review of the Piezoelectric Electromechanical Impedance Based Structural Health Monitoring Technique for Engineering Structures. *Sensors* **2018**, *18*, 1307. [CrossRef] [PubMed]
3. Huynh, T.-C.; Dang, N.-L.; Kim, J.-T. Advances and challenges in impedance-based structural health monitoring. *Struct. Monit. Maint.* **2017**, *4*, 301–329. [CrossRef]
4. Lopes, V.; Park, G.; Cudney, H.H.; Inman, D.J. Impedance-Based Structural Health Monitoring with Artificial Neural Networks. *J. Intell. Mater. Syst. Struct.* **2016**, *11*, 206–214. [CrossRef]

5. Min, J.; Park, S.; Yun, C.-B. Impedance-based structural health monitoring using neural networks for autonomous frequency range selection. *Smart Mater. Struct.* **2010**, *19*, 125011. [CrossRef]
6. Min, J.; Park, S.; Yun, C.-B.; Lee, C.-G.; Lee, C. Impedance-based structural health monitoring incorporating neural network technique for identification of damage type and severity. *Eng. Struct.* **2012**, *39*, 210–220. [CrossRef]
7. Park, G.; Sohn, H.; Farrar, C.R.; Inman, D.J. Overview of piezoelectric impedance-based health monitoring and path forward. *Shock. Vib. Dig.* **2003**, *35*, 451–464. [CrossRef]
8. Park, G.; Cudney, H.H.; Inman, D.J. Feasibility of using impedance-based damage assessment for pipeline structures. *Earthq. Eng. Struct. Dyn.* **2001**, *30*, 1463–1474. [CrossRef]
9. Le, T.-C.; Luu, T.-H.-T.; Nguyen, H.-P.; Nguyen, T.-H.; Ho, D.-D.; Huynh, T.-C. Piezoelectric Impedance-Based Structural Health Monitoring of Wind Turbine Structures: Current Status and Future Perspectives. *Energies* **2022**, *15*, 5459. [CrossRef]
10. Burgoyne, C.; Scantlebury, R. Lessons learned from the bridge collapse in Palau. *Proc. Inst. Civ. Eng.-Civ. Eng.* **2008**, *161*, 28–34. [CrossRef]
11. Nguyen, K.-D.; Kim, J.-T.; Park, Y.-H. Multiscale structural health monitoring of cable-anchorage system using piezoelectric PZT sensors. *Int. J. Distrib. Sens. Netw.* **2013**, *9*, 254785. [CrossRef]
12. Min, J.; Yun, C.-B.; Hong, J.-W. An electromechanical impedance-based method for tensile force estimation and damage diagnosis of post-tensioning systems. *Smart Struct. Syst.* **2016**, *17*, 107–122. [CrossRef]
13. Huynh, T.-C.; Lee, K.-S.; Kim, J.-T. Local dynamic characteristics of PZT impedance interface on tendon anchorage under prestress force variation. *Smart Struct. Syst.* **2015**, *15*, 375–393. [CrossRef]
14. Kim, J.-T.; Park, J.-H.; Hong, D.-S.; Park, W.-S. Hybrid health monitoring of prestressed concrete girder bridges by sequential vibration-impedance approaches. *Eng. Struct.* **2010**, *32*, 115–128. [CrossRef]
15. Nguyen, K.-D.; Kim, J.-T. Smart PZT-interface for wireless impedance-based prestress-loss monitoring in tendon-anchorage connection. *Smart Struct. Syst.* **2012**, *9*, 489–504. [CrossRef]
16. Nguyen, T.-H.; Phan, T.T.V.; Le, T.-C.; Ho, D.-D.; Huynh, T.-C. Numerical Simulation of Single-Point Mount PZT-Interface for Admittance-Based Anchor Force Monitoring. *Buildings* **2021**, *11*, 550. [CrossRef]
17. Nguyen, T.-T.; Hoang, N.-D.; Nguyen, T.-H.; Huynh, T.-C. Analytical impedance model for piezoelectric-based smart Strand and its feasibility for prestress force prediction. *Struct. Control Health Monit.* **2022**, *29*, e3061. [CrossRef]
18. Nguyen, T.-T.; Tuong Vy Phan, T.; Ho, D.-D.; Man Singh Pradhan, A.; Huynh, T.-C. Deep learning-based autonomous damage-sensitive feature extraction for impedance-based prestress monitoring. *Eng. Struct.* **2022**, *259*, 114172. [CrossRef]
19. Dang, N.-L.; Huynh, T.-C.; Pham, Q.-Q.; Lee, S.-Y.; Kim, J.-T. Damage-sensitive impedance sensor placement on multi-strand anchorage based on local stress variation analysis. *Struct. Control Health Monit.* **2020**, *27*, e2547. [CrossRef]
20. Pham, Q.-Q.; Dang, N.-L.; Ta, Q.-B.; Kim, J.-T. Optimal Localization of Smart Aggregate Sensor for Concrete Damage Monitoring in PSC Anchorage Zone. *Sensors* **2021**, *21*, 6337. [CrossRef]
21. Pham, Q.-Q.; Ta, Q.-B.; Kim, J.-T. Capsule-Like Smart Aggregate with Pre-Determined Frequency Range for Impedance-Based Stress Monitoring. *Sensors* **2023**, *23*, 434. [CrossRef] [PubMed]
22. Shi, Z.; Sun, Z.; Yang, S.; Zhou, K. Fatigue Performance of Butt-Welded Tensile Plate Cable-Girder Anchorages of Long-Span Cable-Stayed Steel Box Girder Railway Bridges. *J. Bridge Eng.* **2021**, *26*, 04020108. [CrossRef]
23. Wei, X.; Qiang, S. Fatigue performance of anchorage zone for long-span single pylon cable-stayed bridge. *J. Southwest Jiaotong Univ.* **2011**, *46*, 940–945. [CrossRef]
24. Tenreiro, A.F.G.; Lopes, A.M.; da Silva, L.F.; Amorim, J.D. Effect of mechanical properties and geometric dimensions on electromechanical impedance signatures for adhesive joint integrity monitoring. *Mech. Adv. Mater. Struct.* **2022**, 1–16. [CrossRef]
25. Nguyen, T.-T.; Ho, D.-D.; Huynh, T.-C. Electromechanical impedance-based prestress force prediction method using resonant frequency shifts and finite element modelling. *Dev. Built Environ.* **2022**, *12*, 100089. [CrossRef]
26. Ai, D.; Du, L.; Li, H.; Zhu, H. Corrosion damage identification for reinforced concrete beam using embedded piezoelectric transducer: Numerical simulation. *Measurement* **2022**, *192*, 110925. [CrossRef]
27. Sikdar, S.; Singh, S.K.; Malinowski, P.; Ostachowicz, W. Electromechanical impedance based debond localisation in a composite sandwich structure. *J. Intell. Mater. Syst. Struct.* **2022**, *33*, 1487–1496. [CrossRef]
28. Moharana, S.; Sevugaperumal Arun, V. Piezo impedance-based monitoring of loosening of bolts: Experimental and numerical study. *J. Intell. Mater. Syst. Struct.* **2022**, *33*, 1056–1071. [CrossRef]
29. Liang, C.; Sun, F.P.; Rogers, C.A. Coupled Electro-Mechanical Analysis of Adaptive Material Systems—Determination of the Actuator Power Consumption and System Energy Transfer. *J. Intell. Mater. Syst. Struct.* **1994**, *5*, 12–20. [CrossRef]
30. Park, S.; Yun, C.B.; Inman, D.J. Structural health monitoring using electro-mechanical impedance sensors. *Fatigue Fract. Eng. Mater. Struct.* **2008**, *31*, 714–724. [CrossRef]
31. Xu, Y.; Liu, G. A modified electro-mechanical impedance model of piezoelectric actuator-sensors for debonding detection of composite patches. *J. Intell. Mater. Syst. Struct.* **2002**, *13*, 389–396. [CrossRef]
32. Ritdumrongkul, S.; Abe, M.; Fujino, Y.; Miyashita, T. Quantitative health monitoring of bolted joints using a piezoceramic actuator–sensor. *Smart Mater. Struct.* **2004**, *13*, 20. [CrossRef]
33. Yan, W.; Chen, W.Q.; Cai, J.B.; Lim, C.W. Quantitative structural damage detection using high-frequency piezoelectric signa-turesvia the reverberation matrix method. *Int. J. Numer. Methods Eng.* **2007**, *71*, 505–528. [CrossRef]

34. Giurgiutiu, V.; Zagrai, A.; Bao, J.J. Piezoelectric wafer embedded active sensors for aging aircraft structural health monitoring. *Struct. Health Monit.* **2002**, *1*, 41–61. [CrossRef]
35. Park, G.; Inman, D.J. Structural health monitoring using piezoelectric impedance measurements. *Philos. Trans. A Math. Phys. Eng. Sci.* **2007**, *365*, 373–392. [CrossRef] [PubMed]
36. Wandowski, T.; Malinowski, P.; Radzienski, M.; Opoka, S.; Ostachowicz, W. Methods for Assessment of Composite Aerospace Structures. In *Smart Structures and Materials: Selected Papers from the 7th ECCOMAS Thematic Conference on Smart Structures and Materials*; Araujo, A.L., Mota Soares, C.A., Eds.; Springer International Publishing: Cham, Switzerland, 2017. [CrossRef]
37. Baptista, F.G.; Budoya, D.E.; Almeida, V.A.D.d.; Ulson, J.A.C. An Experimental Study on the Effect of Temperature on Piezoelectric Sensors for Impedance-Based Structural Health Monitoring. *Sensors* **2014**, *14*, 1208–1227. [CrossRef] [PubMed]
38. Uddin, M.N.; Islam, M.S.; Sampe, J.; Ali, S.H.M.; Bhuyan, M.S. Design and simulation of piezoelectric cantilever beam based on mechanical vibration for energy harvesting application. In Proceedings of the 2016 International Conference on Innovations in Science, Engineering and Technology (ICISET), Chittagong, Bangladesh, 28–29 October 2016; pp. 1–4. [CrossRef]
39. Mansoor, M.B.; Köble, S.; Wong, T.W.; Woias, P.; Goldschmidtböing, F. Design, Characterization and Sensitivity Analysis of a Piezoelectric Ceramic/Metal Composite Transducer. *Micromachines* **2017**, *8*, 271. [CrossRef]
40. Dang, N.-L.; Huynh, T.-C.; Kim, J.-T. Local strand-breakage detection in multi-strand anchorage system using an impedance-based stress monitoring method—Feasibility study. *Sensors* **2019**, *19*, 1054. [CrossRef] [PubMed]
41. Huynh, T.-C.; Lee, S.-Y.; Dang, N.-L.; Kim, J.-T. Sensing region characteristics of smart piezoelectric interface for damage monitoring in plate-like structures. *Sensors* **2019**, *19*, 1377. [CrossRef]
42. Huynh, T.-C.; Park, Y.-H.; Park, J.-H.; Kim, J.-T. Feasibility Verification of Mountable PZT-Interface for Impedance Monitoring in Tendon-Anchorage. *Shock. Vib.* **2015**, *2015*, 11. [CrossRef]
43. Kim, J.-T.; Nguyen, K.-D.; Park, J.-H. Wireless impedance sensor node and interface washer for damage monitoring in structural connections. *Adv. Struct. Eng.* **2012**, *15*, 871–885. [CrossRef]
44. Overly, T.G.S.; Park, G.; Farinholt, K.M.; Farrar, C.R. Development of an extremely compact impedance-based wireless sensing device. *Smart Mater. Struct.* **2008**, *17*, 065011. [CrossRef]
45. Park, S.; Shin, H.-H.; Yun, C.-B. Wireless impedance sensor nodes for functions of structural damage identification and sensor self-diagnosis. *Smart Mater. Struct.* **2009**, *18*, 055001. [CrossRef]
46. Park, J.-H.; Kim, J.-T.; Hong, D.-S.; Mascarenas, D.; Lynch, J.P. Autonomous smart sensor nodes for global and local damage detection of prestressed concrete bridges based on accelerations and impedance measurements. *Smart Struct. Syst.* **2010**, *6*, 711–730. [CrossRef]